UC Irvine

UC Irvine Previously Published Works

Title

Discrete Wavelet Transformation for the Sensitive Detection of Ultrashort Radiation Pulse With Radiation-Induced Acoustics

Permalink

https://escholarship.org/uc/item/7d9519ch

Journal

IEEE Transactions on Radiation and Plasma Medical Sciences, 8(1)

ISSN

2469-7311

Authors

Van Bergen, Rick
Sun, Leshan
Pandey, Prabodh Kumar
et al.

Publication Date

2024

DOI

10.1109/trpms.2023.3314339

Copyright Information

This work is made available under the terms of a Creative Commons Attribution License, available at https://creativecommons.org/licenses/by/4.0/

Peer reviewed

eScholarship.org Powered by the California Digital Library
University of California

Discrete Wavelet Transformation for the Sensitive Detection of Ultrashort Radiation Pulse With Radiation-Induced Acoustics

Rick van Bergen, *Member, IEEE*, Leshan Sun, *Member, IEEE*, Prabodh Kumar Pandey, *Member, IEEE*, Siqi Wang, *Member, IEEE*, Kristina Bjegovic, *Member, IEEE*, Gilberto Gonzalez, *Member, IEEE*, Yong Chen, *Member, IEEE*, Richard Lopata, *Senior Member, IEEE*, and Liangzhong Xiang, *Member, IEEE*

***Abstract*—Radiation-induced acoustics (RIA) shows promise in advancing radiological imaging and radiotherapy dosimetry methods. However, RIA signals often require extensive averaging to achieve reasonable signal-to-noise ratios, which increases patient radiation exposure and limits real-time applications. Therefore, this article proposes a discrete wavelet transform (DWT)-based filtering approach to denoise the RIA signals and avoid extensive averaging. The algorithm was benchmarked against low-pass filters and tested on various types of RIA sources, including low-energy X-rays, high-energy X-rays, and protons. The proposed method significantly reduced the required averages (1000 times less averaging for low-energy X-ray RIA, 32 times less averaging for high-energy X-ray RIA, and four times less averaging for proton RIA) and demonstrated robustness in filtering signals from different sources of radiation. The coif5 wavelet in conjunction with the sqtwolog threshold selection algorithm yielded the best results. The proposed DWT filtering method enables high-quality, automated, and robust filtering of RIA signals, with a performance similar to low-pass filtering, aiding in the clinical translation of radiation-based acoustic imaging for radiology and radiation oncology.**

***Index Terms*—Discrete wavelet filtering, radiation induced acoustics (RIA), radiation monitoring.**

Manuscript received 17 April 2023; revised 2 July 2023; accepted 15 August 2023. Date of publication 12 September 2023; date of current version 3 January 2024. This work was supported in part by the National Institute of Health under Grant R37CA240806; in part by the American Cancer Society under Grant 133697-RSG-19-110-01-CCE; and in part by the UCI Chao Family Comprehensive Cancer Center under Grant P30CA062203. *(Corresponding author: Liangzhong Xiang.)*

This work did not involve human subjects or animals in its research.

Rick van Bergen and Richard Lopata are with the PULS/e Lab Eindhoven, Department of Biomedical Engineering, Eindhoven University of Technology, 5600 MB Eindhoven, The Netherlands (e-mail: r.j.p.v.bergen@tue.nl).

Leshan Sun, Siqi Wang, and Kristina Bjegovic are with the Department of Biomedical Engineering, University of California at Irvine, Irvine, CA 92617 USA.

Prabodh Kumar Pandey is with the Department of Radiological Sciences, University of California at Irvine, Irvine, CA 92617 USA.

Gilberto Gonzalez and Yong Chen are with the Department of Radiation Oncology, University of Oklahoma Health Sciences Center, Oklahoma City, OK 73104 USA.

Liangzhong Xiang is with the Department of Biomedical Engineering and the Department of Radiological Sciences, University of California at Irvine, Irvine, CA 92617 USA, and also with the Beckman Laser Institute and Medical Clinic, University of California at Irvine, Irvine, CA 92612 USA (e-mail: liangzhx@hs.uci.edu).

Color versions of one or more figures in this article are available at https://doi.org/10.1109/TRPMS.2023.3314339.

Digital Object Identifier 10.1109/TRPMS.2023.3314339

I. Introduction

RADIATION has a crucial role in modern medicine for both disease diagnosis and treatment. Since the discovery of X-rays by Wilhelm Roentgen in 1895, radiation has been quickly applied in radiological imaging and cancer treatments. In fact, only three days after the announcement of the X-ray discovery, the E.H. Grubb Company applied X-rays in cancer treatment [1], [2]. In the past 127 years, the development of new radiation sources and detectors has continued to evolve, benefiting both fundamental research and practical applications. However, to fully realize the potential of radiation, better control and measurement of radiation are necessary.

Detection techniques for ultrashort ($<\mu s$) pulsed radiation are of particular interest. Most common radiation detectors have a relatively long response time ($\sim ms$) and are unsuitable for the detection of ultrashort pulses. Our group has been developing radiation-induced acoustic (RIA) technologies specifically for the detection of ultrashort radiation pulses ($<\mu s$) [3], [4], [5], [6]. RIA works by inducing a local temperature rise in the target, resulting in thermoelastic expansion and the creation of pressure waves that can be measured with a piezo-electric transducer [4]. The amplitude of this signal has a linear relation with the radiation absorption and, therefore, the administered dose [7]. RIA has potential applications beyond the biological field, such as in measuring concrete infrastructure and nondestructive testing [4], [8]. Fig. 1 shows the general principle of RIA and its application to various radiation sources. This article will focus on RIA's application to three different sources: 1) low-energy photon beams from *x*-ray imaging; 2) high-energy photon beams from radiotherapy; and 3) therapeutic proton beams [7], [9]. By applying RIA on a low-energy photon beam, it is possible to perform X-ray-induced acoustic computed tomography (XACT), which has proven to be applicable for diagnostic imaging [7]. The absorption-based contrast provided by XACT can offer valuable information about various structures, such as bone mineral density [4], [10], [11], [12], [13]. Furthermore, applying RIA to a 2-D X-ray imaging setup enables 3-D volumetric measurement, which augments the information obtained from a single X-ray exposure [14]. The RIA signals can also be created by a high-energy therapeutic photon beam,

2469-7311 © 2023 IEEE. Personal use is permitted, but republication/redistribution requires IEEE permission.
See https://www.ieee.org/publications/rights/index.html for more information.

Authorized licensed use limited to: Access paid by The UC Irvine Libraries. Downloaded on January 04,2024 at 23:51:20 UTC from IEEE Xplore. Restrictions apply.

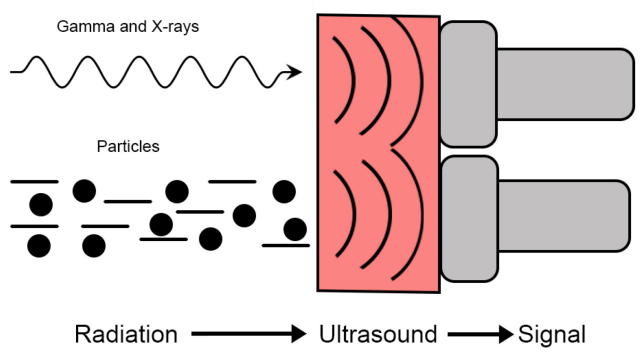

Fig. 1. Generation of ultrasound using various radiation sources, such as low-energy X-rays, high-energy gamma rays, and protons. Piezoelectric transducers are utilized to detect these sound waves and convert them into electrical signals.

enabling real-time in vivo dosimetry during radiotherapy [15], [16], which can reduce treatment margins and improve the quality and effectiveness of radiotherapy [17], [18]. Additionally, proton therapy can benefit from RIA signals through proton acoustic imaging [19], which enables real-time Bragg peak localization in 3-D, allowing for the reduction of the irradiated volume and dose up-scaling, further improving the quality and effectiveness of proton therapy [7], [20], [21], [22].

One problem that arises with RIA is its low-signal-to-noise ratio (SNR) [23], [24], which requires the averaging of multiple acquisitions [7], [25], [26], [27]. However, the downside of averaging is that it may expose the patient to a higher dose, as more than 1000 pulses are required per image. In addition, acquiring a large number of frames per image significantly drops the frame rate, limiting RIA's ability to provide real-time dose information [28]. To address these issues, applying filtering to reduce the number of frames per image is important. However, standard Fourier-based filtering, such as low-pass (LP) filters, falls short in taking time-dependent features into account [29], [30]. Therefore, this article aims to improve signal quality using a wavelet (WL) transform-based denoising algorithm. The wavelet transform expands on Fourier analysis by incorporating time information into the transformed signal [31]. This added detail can result in better-filtering performance and preserve more signal energy [30], [32]. There are two types of wavelet transforms: 1) the continuous wavelet transform (CWT) and 2) the discrete wavelet transform (DWT) as can be seen in Fig. 2 [33]. While both can provide valuable frequency and time distributions, this article focuses on the DWT due to its computational efficiency in a medical context [34]. In literature, wavelet analysis has also been applied to denoise photoacoustic signals [35], [36]. Wavelet analysis has also been successfully employed to denoise protoacoustic signals in a previous study [37]. Specifically, the analyzed signals in that paper originated from accelerometers with very low frequencies (<100 kHz). The signals were processed using a high-pass filter at 10 Hz and a low-pass filter at 100 kHz to enhance their quality before the WL filtering. In this article, we would like to expand on the potential of wavelet denoising by processing data obtained by

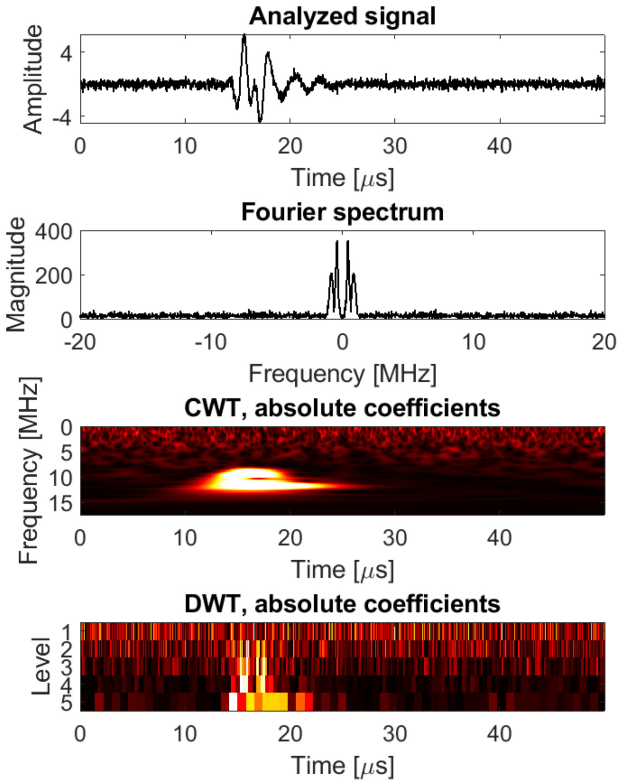

Fig. 2. Comparison of Fourier, CWT, and DWT analyses on an RIA signal. The first figure displays the signal, while the second figure shows the Fourier spectrum providing frequency information only. The third figure presents the CWT scalogram, showing both frequency and time information. The fourth figure displays the 5-level DWT decomposition, which is a sparse representation of the scalogram.

more types of radiation and transducers. The hyperparameters of the workflow will be determined through simulation and tested on data generated from low-energy photons, high-energy photons, and protons to assess their quality and robustness. The main goal is to produce a workflow that is able to perform equal to or better than the LP filtering method.

II. Materials and Methods

Wavelets allow for selective filtering by extracting temporal and frequency information from a signal [30]. To perform wavelet denoising, the DWT is used to perform wavelet analysis, yielding multiple levels of coefficients. These coefficients are then thresholded and used to synthesize a filtered signal using the inverse DWT (IDWT) [38].

The first step in the filtering procedure is to apply the 1-D DWT to each radio frequency (RF) line in the sinogram [Fig. 3(a)]. A sinogram is a 2-D representation of the acoustic signal measured by the transducer, with each row representing the signal of one element. Before filtering, the signal is truncated to exclude the head wave resulting from radiation interacting with the transducer. The 1-D DWT is chosen over the 2-D DWT to avoid interchannel crosstalk, and the mother wavelet is selected through a grid search (Appendix C) [39], [40]. The wavelet and scaling functions represent high- and low-pass filters, respectively [41], and can be arranged to decompose the signal into multiple

Authorized licensed use limited to: Access paid by The UC Irvine Libraries. Downloaded on January 04,2024 at 23:51:20 UTC from IEEE Xplore. Restrictions apply.

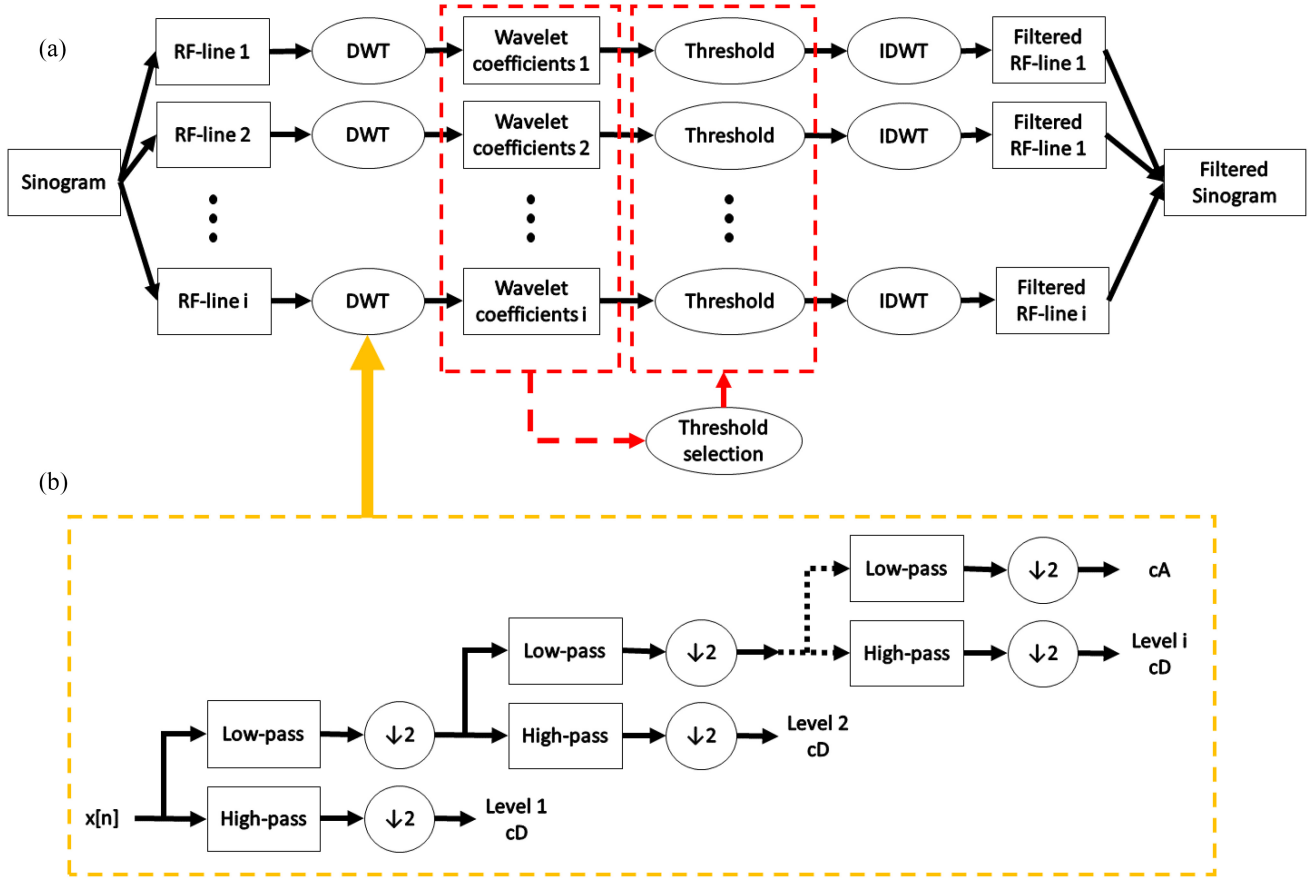

Fig. 3. (a) Denoising workflow for sinograms. It involves performing DWT on each RF line to obtain wavelet coefficients, calculating threshold values for each RF line, applying them to the cD, and reconstructing the RF lines with the IDWT. (b) Illustrates the DWT algorithm, which uses a filter bank of high- and low-pass filters followed by downsampling to obtain cD and cA sets at each level up to a predetermined level i.

levels of detail coefficients (cD) and one set of approximation coefficients (cA), all containing distinct frequency bands [Fig. 3(b)]. The number of levels used in wavelet decomposition determines which frequency bands are analyzed. A higher level means a higher scaling of the mother wavelet and the inclusion of finer low-frequency bands [30]. To ensure a versatile model, the maximum possible decomposition level was calculated using the following [42]:

$$\text{Level} = \text{fix}\left(\log_2\left(\frac{l_x}{l_w - 1}\right)\right). \tag{1}$$

Here, the fix rounds the fraction toward zero, the $\log_2$ accounts for downsampling, and l_x and l_w are the signal and wavelet length, respectively. This method may overestimate the level needed for denoising, but adding more levels after reaching an appropriate one was found to not improve nor worsen denoising [43]. The cD were thresholded to remove noise, using level-dependent threshold estimation and noise estimate rescaling, as the noise's standard deviation varied between levels [44], [45]. To obtain level-dependent thresholds for all RF lines, the level-dependent thresholds were first calculated for individual RF lines and then combined using the mean. The selection of the threshold algorithm is a hyperparameter and is further discussed in Appendix C. Typically, noise is concentrated in the first few levels of detail coefficients [43]. Therefore, the first two levels of cD were set to zero. For filtering of the other levels, two common thresholding rules are hard and soft thresholding [38]. In hard thresholding, all values whose absolute value is lower than the threshold are set to zero, leading to the introduction of discontinuities. Soft thresholding is an alternative, but it shifts the nonthresholded coefficients toward zero, which can cause an underestimation of the dose in the context of RIA [29]. Therefore, hard thresholding was used for the wavelet coefficients.

To address the issues encountered in signal processing due to hard thresholding, a mathematical morphological dilation was used. This involved applying the hard threshold to the cD coefficients and then creating a mask for each decomposition level to identify the thresholded and nonthresholded regions. The next step was to dilate these masks and multiply them with the original nonthresholded cD, effectively applying the threshold. To perform the dilation, the following equation was utilized [46]:

$$\delta(X_i) = X_i \oplus S = \{x + s | x \in X_i \wedge s \in S\}. \tag{2}$$

Here, $\oplus$ represents the dilation operator. X_i denotes the threshold mask of the ith cD level and has a size of $1 \times N_i$ where N_i is the length of the cD in level i. S is a morphological structure element, which is an array with a size of $1 \times L$ containing only ones. The dilatation window size

Authorized licensed use limited to: Access paid by The UC Irvine Libraries. Downloaded on January 04,2024 at 23:51:20 UTC from IEEE Xplore. Restrictions apply.

remains constant for all levels of cD. x and s are the elements of X_i and S, respectively. The size of the structure element, L, significantly affects the dilation performance. When L is large, limited values are thresholded, whereas when L is small, no region adjacent to nonthresholded sections is dilated. This hyperparameter was chosen based on a grid search, for which more details will be provided in Appendix C. After the thresholding is applied, the IDWT is performed on the thresholded coefficients to synthesize the RF lines and obtain the filtered sinogram [38]. The filtered sinograms were reconstructed to visually asses the filtering performance using a back-projection algorithm [47].

One simulated and three experimental datasets were used to test the performance of the filter. The XACT experiment was simulated using the k-Wave simulation toolbox in MATLAB [48], [49]. The simulated transducer was a 16×16 matrix array with a 1-MHz center frequency and 40-MHz sampling frequency, matching the characteristics of the transducer used in the XACT experiment. The simulation was performed on a lead cross phantom, which has a high-x-ray absorption, leading to high contrast in the image. The initial pressure was applied to all phantom voxels, eliminating the need to model radiation transport and interactions. The simulated acoustic signal was filtered using a band-pass filter to emulate the bandwidth-limited signal seen in experimental acoustic signals [50]. The simulation provided a controlled environment to test filter performance and optimize hyperparameters. Additionally, it allowed for the examination of denoising performance on suboptimal datasets with varying noise levels. To incorporate the desired noise levels, we utilized the "addNoise" function from the k-wave toolbox, introducing white noise with varying SNRs. It is important to note that in real experimental scenarios, a significant portion of the noise stems from electromagnetic interference, which exhibits a broad spectrum of frequencies and amplitudes. Gaussian white noise serves as a simplified representation of this complex experimental noise. In our study, we employed three simulated datasets with SNRs of 10, 15, and 20. These SNR values were selected to accurately reflect low-SNR experimental data commonly encountered in practice. By incorporating these noise levels, we aimed to provide a realistic representation of the challenges associated with noise in the analyzed signals. The output from the simulation were sinograms of the signal received by the transducer, with a size of $N_{ch} \times N_s$, where N_{ch} is the number of channels and N_s is the number of samples. The XACT experiment was performed by irradiating a lead cross suspended in water-based 3% agar (BactoTM, Becton) with low-energy X-ray photons. The geometry of the cross coincided with the cross used in the simulations. Appendix B Fig. 9(a) shows a schematic representation of the imaging setup. In the figure, the transducer and the radiation source are on the same axis. In the experiment, a 150-kV X-ray generator (XR200, Golden Engineering) irradiated the cross, operating at a repetition rate of 10 Hz and a pulse width of 50 ns. To perform 3-D imaging, the generated acoustic waves were measured with a 16×16 channel matrix array transducer (NDT probe, Doppler Company Ltd.) with a 1-MHz center frequency, a 60% bandwidth, and a sampling frequency of 40 MHz. After the acquisition, a data acquisition device (Legion ADC, Photosound Technologies Inc.) with a preamplifier was used to amplify the signal. The data generated by the matrix transducer will be processed as a $N_{ch} \times N_s$ sinogram.

The data from the high-energy photon experiment was obtained using a linear particle accelerator (LINAC) (Synergy, Elekta) firing a 10 MV photon beam with a repetition rate of 200 Hz. The acoustic signal was captured using a point transducer (videoscan, Olympus IDT) with a 500-kHz center frequency. The signal captured by the point transducer was amplified by a 60-dB preamplifier (Olympus) and a 200 v/v preamplifier (Stanford Research Systems), which increased signal levels and applied a 1-MHz low-pass filter and a 10-kHz high-pass filter. The experiment irradiated a water tank to measure the LINAC beam profile, collimated into a 4x6cm field. The ultrasound sensor was perpendicular to the LINAC beam. A setup schematic is provided in Appendix B Fig. 9(b). Since a single channel is being used, only one RF signal will be processed as opposed to the sinograms of the other datasets. As a consequence, no reconstructions could be performed with this data.

In the proton acoustic experiment, a proton beam irradiated a water tank. The main goal of the experiment was to visualize the proton Bragg peak. Considering the orientation of the different components of this setup, the protons are fired toward the transducer, shown schematically in Appendix B Fig. 9(c). The transducer used was the same 16×16 matrix array as in the XACT experiment. The Bragg peak image was created using an 87-MeV proton beam with a 4-μs pulse width generated by a proton accelerator (MEvion). The peak was positioned 6 cm away from the transducer surface.

To test the performance of the WL filter, the results of all datasets will be compared to an LP filter. The LP filter was applied to each individual line of the sinogram to prevent cross-talk. The cut-off frequency for the LP filter was determined for each dataset based on the CWT scalograms. These scalograms give a broader representation of the frequency content compared to Fourier spectra and therefore facilitate cut-off frequency selection. Three metrics were used to quantify the denoising results: 1) the mean squared error (MSE); 2) peak SNR (PSNR); and 3) the correlation coefficient (CC). The MSE can be calculated with

$$\text{MSE} = \sum_{i=1}^{N} \frac{(y_i - x_i)^2}{N}. \tag{3}$$

Here, x is the clean signal, y is the filtered signal, and N is the number of samples. The MSE provides the difference between x and y.

The PSNR can be calculated using [51]

$$\text{PSNR} = 10 \cdot \log_{10}\left(\frac{\text{MAX}_I^2}{\text{MSE}}\right). \tag{4}$$

The MSE was calculated using (3). The MAX_I represents the range of values occurring in the ground truth (GT). Note that comparisons between different datasets with the PSNR are

Authorized licensed use limited to: Access paid by The UC Irvine Libraries. Downloaded on January 04,2024 at 23:51:20 UTC from IEEE Xplore. Restrictions apply.

only valid when both use a similar range. The PSNR tells something about how much noise is present with respect to the signal, making it more intuitive than the MSE, which only measures the difference between the approximation and the signal [51].

Finally, the CC between the clean and the filtered signal was considered [52]

$$r = \frac{1}{N-1}\sum_{i=1}^{N}\left(\frac{x-\bar{x}}{\sigma_x}\right)\left(\frac{y-\bar{y}}{\sigma_y}\right). \tag{5}$$

In this equation, x and y are the GT and the filtered signal, respectively. N denotes the number of samples. Furthermore, $\bar{x}$ and σ_x are the mean and standard deviation of x, and $\bar{y}$ and σ_x are the mean and standard deviation of y.

The evaluation metrics will be computed for the noisy sinograms, LP-filtered sinograms, and WL-filtered sinograms in comparison to the GT. Since the high-energy photon dataset only has one RF line, the metrics will be computed for a single signal. For the experimental datasets, the GT is defined as the signal obtained with the maximum number of averages. However, the signal quality for the therapeutic photon and proton datasets is expected to be lower than that of the XACT datasets, which could make single-shot imaging challenging. Therefore, an analysis will be conducted to determine the minimum number of averages required to obtain a representative image. In addition, if there is a significant time dependence on the similarity between the signal and the GT, the metrics calculated on the sinogram may not be accurate. To address this issue, the MSE, CC, and PSNR will be computed on the z-slices of the reconstructed volumes of the filtered and averaged data. These 3-D volumes will be obtained using a standard back-projection algorithm [47]. The decision to use the z-slices is based on their time-invariant nature and the ability to provide information about how filtering quality changes as a function of depth.

To achieve optimal WL filtering, several hyperparameters must be selected. The maximal decomposition level is fixed, but the mother wavelet, threshold selection algorithm, and dilation structure element size need to be determined. The mother wavelet selection is critical in filtering outcome and is generally the one with the highest correlation with the signal [40]. However, interactions between hyperparameters can lead to this criterion not providing the best solution. Other wavelet properties, such as phase, vanishing moments, and orthogonality, can also affect denoising [30].

To find the optimal wavelet for denoising, a grid search of parameters on the simulation data is performed [53]. Simulation data is preferred as it has a nonaveraged GT. The denoising is carried out on the simulation data with all possible combinations of hyperparameters, and the results are quantified using MSE, PSNR, and CC with respect to the GT. The best-performing combination of hyperparameters is used to denoise the data from other experiments. The wavelet families considered in the grid search are Daubechies (db), Symlets (sym), Coiflets (coif), Biorthogonal (bior), and Reverse Biorthogonal (rbio) families [30]. The threshold selection methods considered are sqtwolog, rigrsure, heursure, and minimaxi, based on the availability of the MATLAB wavelet toolbox. The sqtwolog threshold can be calculated using the following [38]:

$$\mathrm{th}_j = \sigma_j\sqrt{2\log\left(N_j\right)}. \tag{6}$$

In the equation, N_j is the number of cD in the jth decomposition level, and σ_j is defined to be the mean absolute deviation (MAD) and can be calculated using

$$\sigma_j = \frac{\mathrm{MAD}_j}{0.6745} = \frac{\mathrm{median}\left(|\omega_j|\right)}{0.6745}. \tag{7}$$

In (7), ω_j denotes the level j cD, and the 0.6745 is derived from the 75% percentile of a Gaussian distribution.

The rigrsure threshold is based on Stein's unbiased risk estimate (SURE) and can be calculated using the following [54], [55]:

$$\mathrm{th}_j = \sigma_j\sqrt{\omega_{j,b}}. \tag{8}$$

In (8), the σ_j is the standard deviation of the jth level of detail coefficients, and $\omega_{j,b}$ is the squared wavelet coefficient (b) with minimal risk for the jth level.

The heursure algorithm is a heuristic combination of the aforementioned sqtwolog and rigrsure algorithms. It was found that for a low SNR, the rigrsure estimate is not reliable, and therefore, in that situation, heursure uses the sqtwolog [38], [54].

The final threshold that is included in the analysis is the minimax threshold, which is calculated using the following [38], [56]:

$$\mathrm{th}_j = \begin{cases} \sigma_j\left(0.3936 + 0.10829\log_2 N_j\right), & N_j > 32 \\ 0, & N_j < 32 \end{cases}. \tag{9}$$

In (9), σ_j is the noise estimate of the jth decomposition level and is calculated using (7). Furthermore, N is the number of cD in level j.

III. Results

XACT imaging is limited by its extremely low SNR for biomedical applications [25], [57]. The proposed filtering architecture was tested on an XACT dataset and compared to an LP filter with a cut-off frequency of 1.8 MHz (see the scalogram analysis in Appendix A Fig. 8(b). Furthermore, the GT was the signal acquired after 1000 averages. The filtering process was applied to each ultrasound element and the resulting signals (Fig. 4) were reconstructed using the back projection algorithm for XACT imaging [Fig. 5(a)]. The performance of the filter was also evaluated by computing the metrics for each slice, as shown in Fig. 5(b). The slice-dependent metrics indicated that the WL and LP filters decreased the MSE, increased the CC, and increased the PSNR compared to the noisy data. Moreover, the WL outperformed the LP filter in all metrics up to slice 27, but beyond slice 27, the LP filter provided better approximations to the GT. Notably, Fig. 5 shows periodic improvements in the metrics that coincide with the reflected reconstructions. The MIP of the y–z plane of the GT in Fig. 5(b) (bottom) displays reflections around slices 25, 33, 40, 49, and 55. The reflections, origi-

Authorized licensed use limited to: Access paid by The UC Irvine Libraries. Downloaded on January 04,2024 at 23:51:20 UTC from IEEE Xplore. Restrictions apply.

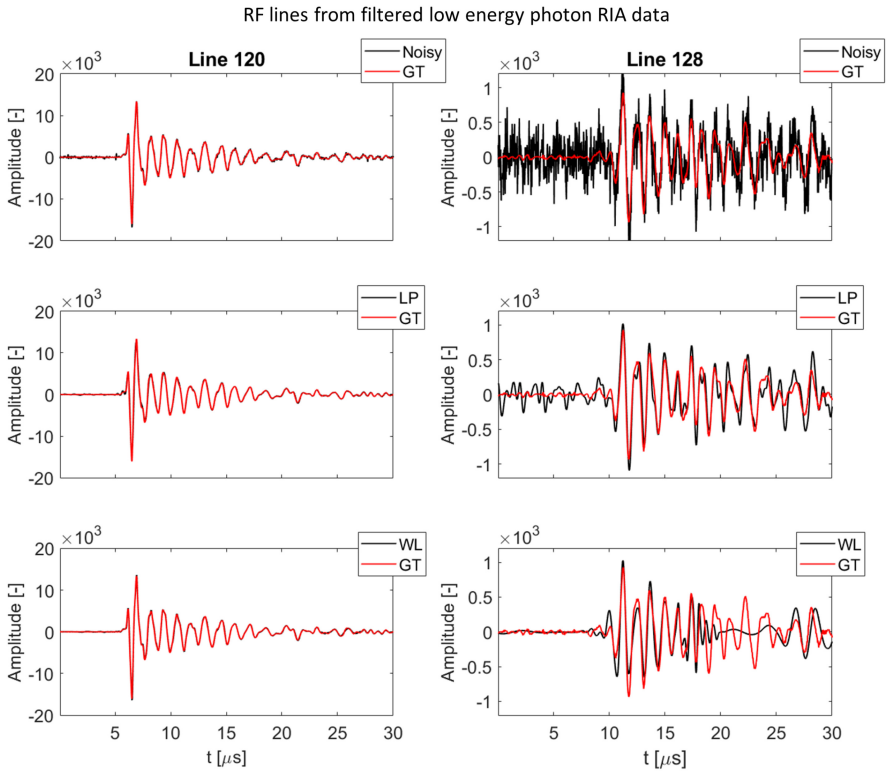

Fig. 4. Filtered RF signals of transducer element 120 and 128 for the experimental single-shot XACT data after filtering. These signals are overlaid on the averaged data.

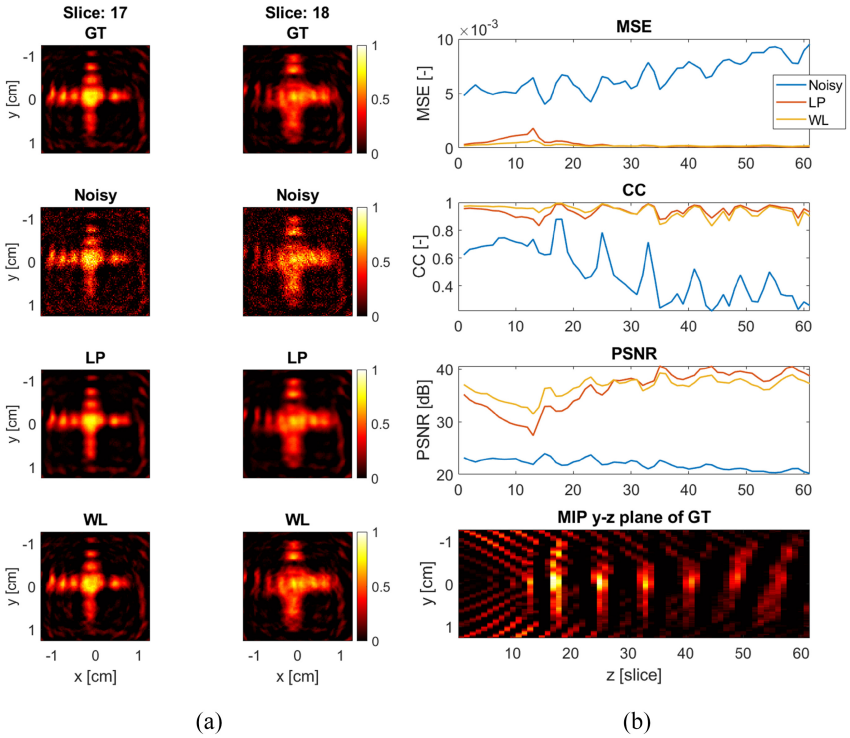

Fig. 5. (a) Displays the reconstruction of the XACT experimental data, with slices 17 and 18 specifically highlighted as they both include the tilted cross. The data was normalized for ease of visualization. (b) Demonstrates the calculation of MSE, CC, and PSNR for each slice individually, and also provides a y–z MIP for comparison between the reconstruction and the metrics.

nating from the sound reflecting in the lead cross, are more distorted and have lower amplitudes at larger depths and need further removal in future research. In conclusion, both methods enable single-shot measurements, as demonstrated in signal processing, and the WL filter can achieve similar or better performance than LP filtering in removing unwanted noise

Authorized licensed use limited to: Access paid by The UC Irvine Libraries. Downloaded on January 04,2024 at 23:51:20 UTC from IEEE Xplore. Restrictions apply.

(a)

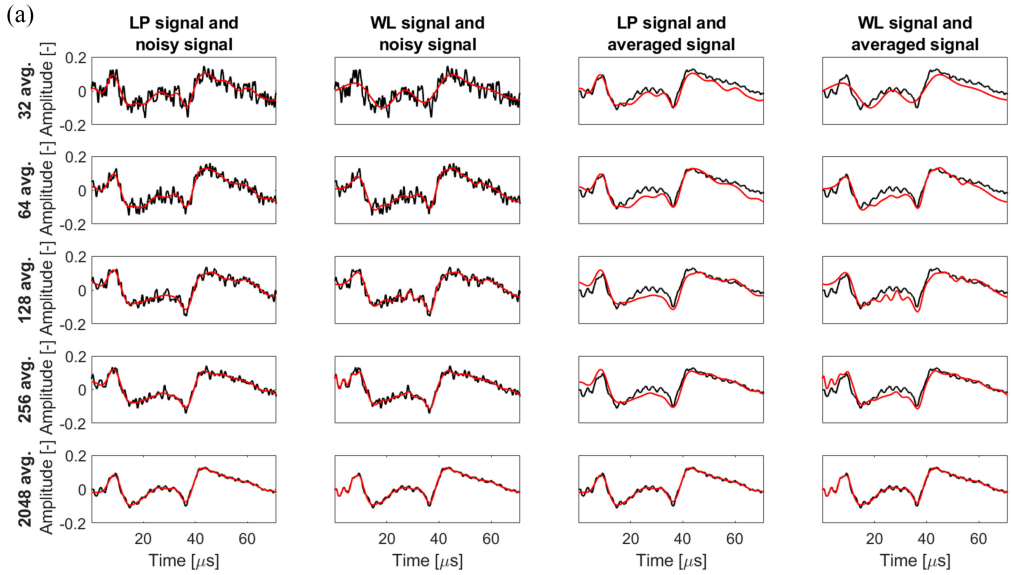

(b)

	Noisy			LP			WL		
Averages	MSE($\times 10^{-4}$)	CC	PSNR [dB]	MSE($\times 10^{-4}$)	CC	PSNR [dB]	MSE($\times 10^{-4}$)	CC	PSNR [dB]
32	17.1	0.844	9.90	8.02	0.951	13.19	11.11	0.907	11.78
64	12.8	0.928	11.16	8.93	0.961	12.72	9.27	0.958	12.56
128	10.1	0.907	12.20	7.77	0.926	13.33	8.34	0.920	13.02
256	6.9	0.927	13.81	6.05	0.933	14.41	6.26	0.931	14.26
2048	-	-	-	0.68	0.990	23.89	0.61	0.991	24.41

(c)

	Noisy			LP			WL		
Averages	MSE ($\times 10^{-4}$)	CC	PSNR [dB]	MSE ($\times 10^{-4}$)	CC	PSNR [dB]	MSE ($\times 10^{-4}$)	CC	PSNR [dB]
32	17.54	0.837	9.50	7.45	0.958	13.22	10.26	0.917	11.84
64	13.08	0.926	10.78	8.34	0.969	12.73	8.65	0.967	12.57
128	10.79	0.898	11.67	7.18	0.934	13.45	7.92	0.926	13.03
256	7.65	0.919	13.11	5.44	0.942	14.59	5.80	0.937	14.31
2048	0.68	0.990	23.60	-	-	-	0.10	0.999	32.14

Fig. 6. (a) Presents, the signal of transducer element 120 of the high-energy photon RIA dataset is displayed as a function of time. (b) Compares the denoising performance of the LP and WL filters with several levels of averages and the maximum averaged signal, referred to as GT, which is the data after 2048 averages. (c) Presents a table of the same metrics but calculated with respect to the LP-filtered data of 2048 averages.

further improving the image reconstruction quality in XACT imaging.

The low SNR of RIA imaging during radiation therapy is identified as a limiting factor for dose sensitivity [4], [6], [15]. To address this, the effectiveness of WL and LP filters in reducing signal averaging is evaluated using X-ray-induced acoustic signals from a clinical medical LINAC. The X-induced acoustic signal is visible between 150 and 200 μs, showing a W-shaped signal, as seen in Fig. 6(a). A cut-off frequency of 0.11 MHz is applied to the LP filter (based on Appendix A Fig. 8(c). Since no target was used, the reflections observed in the low-energy photon dataset [Fig. 5(b)] were absent. Therefore, the denoised signals obtained from different numbers of averages using both filtering methods are compared directly to their corresponding noisy data and the quality of the signals is evaluated using various metrics presented in Fig. 6(b) and (c). The results show that both filtering methods outperform the noisy signal in terms of MSE, CC, and PSNR, with LP performing slightly better than WL for most averages except for 2048, where WL is better. This study demonstrates that the WL filter can significantly reduce signal averaging by 32 times for radiotherapy monitoring while performing slightly worse than the LP filter.

Following the testing of the WL filter on the low and high-energy photon datasets, its performance was evaluated on proton-induced acoustic signals. In Fig. 7(a), the signal from ultrasound transducer element 120 is shown after 2000 averages. Despite using the same transducer, the proton-induced acoustic signal has a lower amplitude than the X-ray-induced signal in Fig. 4. Like the high-energy photon data, the proton-induced data is reflection-free, allowing metrics to be calculated on the signals themselves and not on the reconstructions. However, the signal remains noisy even after 2000 averages due to an oscillation present throughout the signal, making the highest available averaged signal inadequate for use as a GT. The data was denoised using different numbers of averages, and Fig. 7(a) shows the signals after LP and WL denoising. The sym8 wavelet was used for denoising the proton-induced acoustic dataset, and a 0.12-MHz cutoff frequency was used for the LP filter based on analysis in Appendix A Fig. 8.

In Fig. 7(a), LP and WL filter performance is shown for various levels of averaged data and the GT (defined as the 2000 averaged dataset). Signals with less than 64 averages were excluded due to poor signal quality. Although 64 and 128 averages still have imperfect filtering, the general trend

Authorized licensed use limited to: Access paid by The UC Irvine Libraries. Downloaded on January 04,2024 at 23:51:20 UTC from IEEE Xplore. Restrictions apply.

(a)

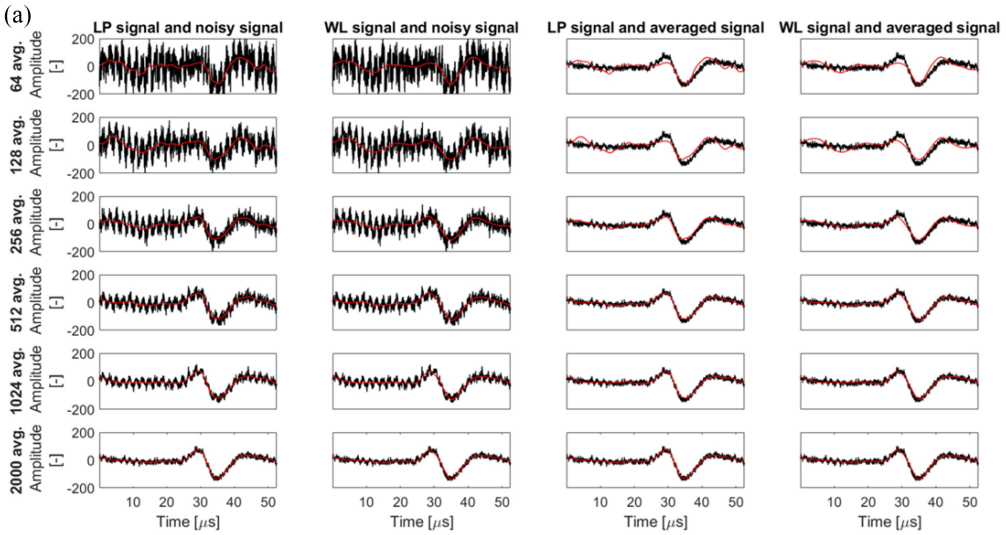

(b)

	Noisy			LP			WL		
Averages	MSE ($\times 10^2$)	CC	PSNR	MSE ($\times 10^2$)	CC	PSNR	MSE ($\times 10^2$)	CC	PSNR
64	119.73	0.384	3.91	37.27	0.517	8.98	36.75	0.519	9.04
128	104.86	0.325	4.49	60.04	0.346	6.91	59.19	0.348	6.97
256	27.23	0.620	10.34	11.65	0.719	14.03	11.73	0.715	14.00
512	9.38	0.821	14.97	3.27	0.904	19.55	3.31	0.902	19.49
1024	3.86	0.904	18.82	2.20	0.931	21.26	2.29	0.928	21.09
2000	-	-	-	1.74	0.945	22.29	1.86	0.942	22.00

(c)

	Noisy			LP			WL		
Averages	MSE ($\times 10^2$)	CC	PSNR	MSE ($\times 10^2$)	CC	PSNR	MSE ($\times 10^2$)	CC	PSNR
64	124.92	0.330	1.90	35.49	0.548	7.36	34.98	0.549	7.43
128	108.68	0.276	2.50	58.26	0.366	5.21	57.40	0.369	5.27
256	30.64	0.555	8.00	9.92	0.760	12.90	9.96	0.757	12.88
512	12.47	0.750	11.90	1.54	0.955	20.97	1.60	0.953	20.83
1024	6.52	0.831	14.72	0.47	0.984	26.18	0.53	0.982	25.62
2000	1.74	0.945	20.46	-	-	-	0.09	0.997	33.26

Fig. 7. (a) Presents, the signal of transducer element 120 of the proton RIA dataset is displayed as a function of time. (b) Compares the denoising performance of the LP and WL filters with several levels of averages and the maximum averaged signal, referred to as GT, which is the data after 2000 averages. (c) Presents a table of the same metrics but calculated with respect to the LP-filtered data of 2000 averages.

of the signal remains. After 256 averages, the signal matches the GT adequately, but the wavelet fails to follow the peak, and the LP fails to follow the dip. Therefore, the minimum number of averages needed for a representative signal after filtering is 512. The differences between WL and LP filtering are minimal. Due to the limited quality of the GT, quantification is performed on the 2000 averaged signal with and without LP filtering, presented in Fig. 7(b) and (c), respectively. Fig. 7(b) shows that LP and WL approaches outperformed noisy data on the PACT with the 2000 averaged dataset as reference. LP and WL performance was consistent for 512, 1024, and 2000 averages, while lower averages led to deterioration in quality. LP slightly outperformed WL as confirmed by Fig. 7(c). Fig. 7 shows that the WL filter can reduce proton-induced acoustic signal averaging (>4 times) and perform similarly to the LP filter for real-time monitoring of proton therapy in clinical translation.

IV. Discussion

In this article, we proposed a WL-based denoising algorithm for RIA imaging, which was tested on simulation and experimental datasets. Our approach involved a grid search on the simulation data to determine the optimal mother wavelet, dilation window size, and threshold selection method for denoising (Appendix C). We found that the sqtwolog threshold selection method combined with a structure element size of 9 for morphological dilation and the coif5 wavelet yielded the best results. We then utilized these hyperparameters to denoise the other datasets. We successfully applied our method to experimental datasets, with the sym8 wavelet used for the PACT dataset. Both LP and WL filtering methods enable single-shot measurements without averaging (Fig. 4), except for the therapeutic photon and proton datasets which require averaging due to the absence of a target resulting in poor signal quality (Figs. 6 and 7). For high-energy photon data, the LP filter provides a signal comparable to 2048 averages after 32 averages, while the WL requires 64 averages due to head-wave overlap and noise. Removing the head wave should allow the WL to perform similarly to the LP. For PACT data, filtering between 256 and 512 averages yields a comparable result to 2000 averages, reducing the required averages by a factor of at least 4. The experimental XACT reconstruction appears dotted due to the back-projection algorithm

Authorized licensed use limited to: Access paid by The UC Irvine Libraries. Downloaded on January 04,2024 at 23:51:20 UTC from IEEE Xplore. Restrictions apply.

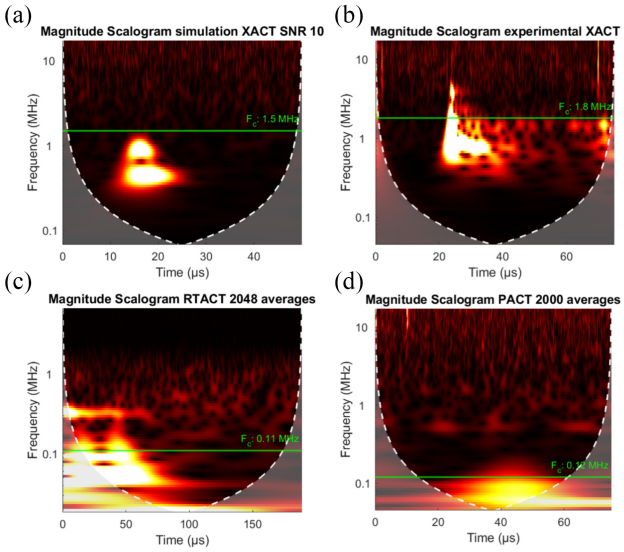

Fig. 8. CWT scalograms of line 120 were used to determine the cut-off frequency for the LP filter for all datasets. Here, (a) is the scalogram for the simulation XACT data with the worst SNR (10) with an LP cutoff of 1.5 MHz; (b) is the scalogram for the experimental XACT data with an LP cutoff of 1.8 MHz; (c) is the scalogram for the high-energy photon data with 2048 averages with an LP cutoff of 0.11 MHz; and (d) is the scalogram for the PACT data with 2000 averages with an LP cutoff of 0.1 MHz.

and the cross being close to the transducer [Fig. 5(a)]. The dotting is not expected to affect the metrics. Reflections in the z-direction are also observed. XACT metrics were calculated for each slice and show the LP outperforming the WL filter after a crossover point. Before the crossover point, the WL is more effective in filtering the signal-less region. The MIP shows that the reflections coincide with increased similarity to the GT, with the filtering methods yielding better performance as the SNR increases in those slices. To achieve better reconstruction, model-based reconstruction or filtering the reflections may be necessary [24]. The RIA signal may be affected by a head wave resulting from the interaction between the radiation and the transducer [Fig. 6(a)]. This artifact significantly impacts denoising and metric calculation accuracy. Cropping was found to be an effective solution for all datasets, except for therapeutic photon data. An automated approach using a background measurement to divide out the head wave may improve the RTACT data quality. The LP filter effectively removes the head wave, while the WL filter preserves noncontinuous signals.

The PACT dataset (Fig. 7) was denoised using the sym8 wavelet instead of the coif5 due to low-frequency oscillation observed in the signal. The sym8 wavelet was found to perform well and has a similar shape to the coif5 wavelet. The coif5 wavelet was chosen for denoising the high-energy photon RIA signals since the low-frequency oscillation was absent. LP and WL filtering showed worse performance in element 120 due to lower-signal intensity and overestimated threshold selection. The single-shot data and averaged data also showed a slight mismatch due to instabilities in the X-ray source, but this is not expected to have a significant impact on the final metric calculations.

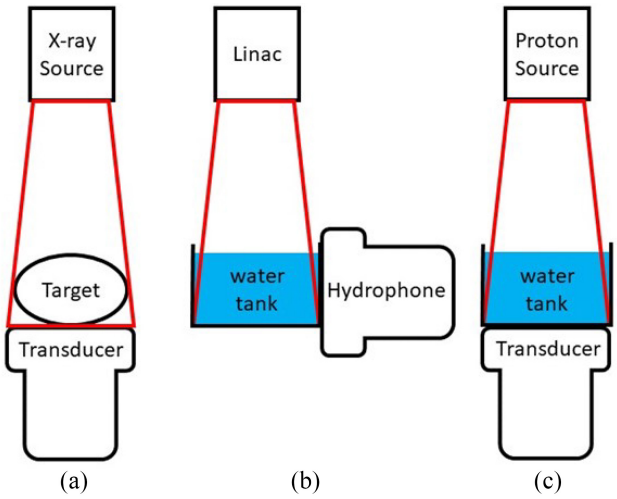

Fig. 9. Schematic representation of the setups used to acquire the signals for all datasets. The main goal of the figure is to present the orientation of the different components. (a) Setup used to acquire the XACT dataset. The simulation dataset was generated using this same geometry. (b) Schematic of the setup used to acquire the therapeutic photon data. (c) Setup used to acquire the PACT measurement.

	SNR = 20	SNR = 15	SNR = 10
Threshold selection	sqtwolog	sqtwolog	sqtwolog
Dilation window size	9	9	9
Wavelet	coif5	coif5	sym8

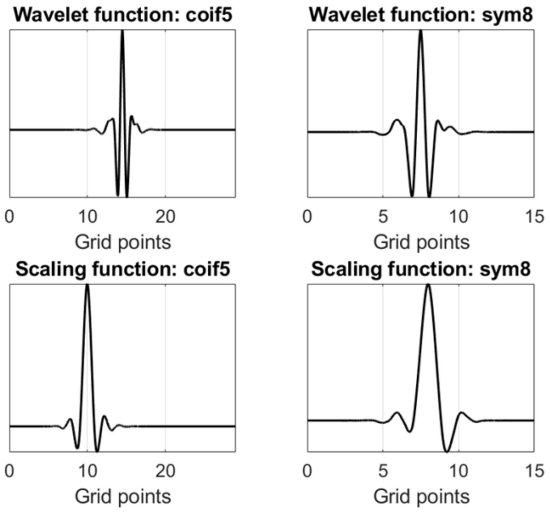

Fig. 10. Top table presents the best-performing hyperparameters for an SNR of 10, 15, and 20. Additionally, the coif5 and sym8 wavelet and scaling functions are provided.

Overall, the WL and LP filters showed similar performance in all the results, but there are some disadvantages to each. The LP filter tended to smooth signals, while the WL filter was more sensitive to low-amplitude RF lines. The WL filter was automated, whereas the LP filter was not. The WL was found to outperform the LP filter in simulated and experimental XACT datasets. For therapeutic photon and proton RIA datasets, the performance of the WL filter was similar

Authorized licensed use limited to: Access paid by The UC Irvine Libraries. Downloaded on January 04,2024 at 23:51:20 UTC from IEEE Xplore. Restrictions apply.

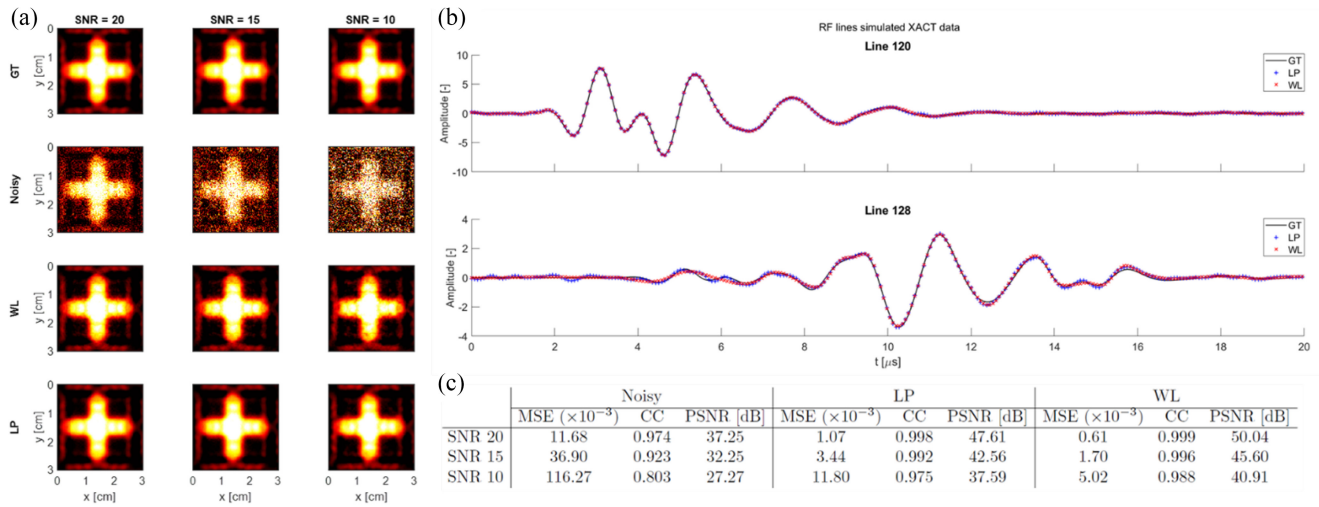

(c)

	Noisy			LP			WL		
	MSE ($\times 10^{-3}$)	CC	PSNR [dB]	MSE ($\times 10^{-3}$)	CC	PSNR [dB]	MSE ($\times 10^{-3}$)	CC	PSNR [dB]
SNR 20	11.68	0.974	37.25	1.07	0.998	47.61	0.61	0.999	50.04
SNR 15	36.90	0.923	32.25	3.44	0.992	42.56	1.70	0.996	45.60
SNR 10	116.27	0.803	27.27	11.80	0.975	37.59	5.02	0.988	40.91

Fig. 11. (a) Reconstruction for the simulated XACT data. The reconstruction was performed for the GT, noisy, LP-filtered, and WL-filtered data. Here, the slice containing the cross is presented. (b) Illustrates the performance of the filter on the RF data from elements 120 and 128. (c) Presents the denoising results using the WL and LP filter in the simulated XACT dataset for an SNR of 10. Furthermore, the GT is added to serve as a reference.

yet slightly worse than the LP filter, and it was challenging to determine which one was truly outperforming the other stemming from the bias introduced by considering the LP filtered data as an additional GT. However, for more complex signals, such as a needle in the proton signal, the WL filter is expected to perform better due to its ability to detect associated frequency features due to the inclusion of time information. Therefore, the filtering method can perform similarly to an LP filter for simple signals and might outperform the LP filter for more complex signals.

V. Conclusion

To conclude, a DWT-based filtering approach for RIA images was proposed, incorporating a novel thresholding method based on morphological dilation to preserve bandwidth-limited signals. The optimal hyperparameters were determined through a grid search on a simulation dataset, leading to the coif5 wavelet, sqtwolog threshold selection, and morphological window size of 9. The method was successfully applied to experimental XACT, therapeutic photon, and PACT datasets, reducing noise and the number of required averages for imaging. WL filtering was found to perform similarly to LP filtering. However, the proposed method is expected to excel in more complex geometries, making it a promising option for clinical RIA imaging.

Appendix A
Sinograms for LP Filter Cut-Off Frequency Selection

See Fig. 8.

Appendix B
Experimental Setups

See Fig. 9.

Appendix C
Grid Search

The best hyperparameters for wavelet-based denoising were determined using a grid search on the simulation data. The parameters included were the mother wavelet, threshold selection method, and the dilation structure element size. The best-performing combinations of hyperparameters for the different noise levels are summarized in the table of Fig. 10. In the table of Fig. 10, sqtwolog is the best-performing threshold selection method for the three noise levels. Furthermore, the best results were obtained with a dilation structure element size of 9. The mother wavelet showed some disagreement between the noise levels. More specifically, the dataset with an SNR of 10 was most accurately denoised using the sym8 wavelet, whereas the other noise levels yielded better results with the coif5 wavelet. The coif5 and the sym8 wavelet and scaling functions are plotted in Fig. 10. It can be seen that both wavelets look similar in shape, but the coif5 wavelet is longer than the sym8. A longer wavelet length might have implications for denoising since a longer wavelet has a lower-maximal decomposition level than a shorter wavelet. The shorter length is expected to lead to better performance of the sym8 wavelet for an SNR of 10. For the SNR of 10, the coif5 wavelet was one of the top-performing wavelets. Therefore, due to the better-overall performance, it was chosen to use the coif5 wavelet to denoise the datasets.

Appendix D
Denoising Results From the Simulated XACT Dataset

The simulated XACT data was denoised with the most optimal hyperparameters, yielding the signals in Fig. 11(b). In Fig. 11(b), the denoising of the simulation dataset with an SNR of 10 is presented for RF lines 120 and 128. These lines were visualized because line 120 is located in the center, and line 128 is located at the edge of the matrix array. The

Authorized licensed use limited to: Access paid by The UC Irvine Libraries. Downloaded on January 04,2024 at 23:51:20 UTC from IEEE Xplore. Restrictions apply.

moment the sound arrives is different for the two channels. The LP filter used a cut-off frequency of 1.5 MHz based on Appendix A. It can be seen that both methods adequately filter the signal in line 120. However, in line 128, slight differences between the methods are observed. Namely, the WL method filters the low-amplitude oscillations to a greater extent than the LP-filtered data. The quality of the denoising of the simulation data was quantified, yielding the metrics in the table of Fig. 11(c). Considering the metrics in the table of Fig. 11(c), the WL and LP filtered data have a lower MSE, higher CC, and higher PSNR than the noisy image. The proposed WL method was found to outperform the LP-filtered data. Furthermore, a decrease in SNR correlates with a reduction in filtering quality. The volumes can be reconstructed from the sinograms. The slices containing the simulated cross are presented in Fig. 11(a). When comparing the reconstructions in Fig. 11(a), several visual observations can be made. In the figure, both the WL and LP methods successfully reduced the noise in the images. Furthermore, it can be appreciated that the WL transform, although marginal, blurs the reconstructed images less than the LP image.

ACKNOWLEDGMENT

The authors declare that they have no known conflicts of interest in terms of competing financial interests or personal relationships that could have an influence or are relevant to the work reported in this article.

Many thanks go to Daniel Green for assistance in signal collection and Debra Galicia Felix for artistic consultations.

REFERENCES

[1] L. R. Holsti, "Development of clinical radiotherapy since 1896," *Acta Oncologica*, vol. 34, no. 8, pp. 995–1003, 2009. [Online]. Available: https://www.tandfonline.com/action/journalInformation?journalCode=ionc20

[2] M. Lederman, "The early history of radiotherapy: 1895–1939," *Int. J. Radiat. Oncol. Biol. Phys.*, vol. 7, no. 5, pp. 639–648, 1981. [Online]. Available: https://pubmed.ncbi.nlm.nih.gov/7024222/

[3] E. Robertson and L. Xiang, "Theranostics with radiation-induced ultrasound emission (TRUE)," *J. Innovat. Opt. Health Sci.*, vol. 11, no. 3, Art. no. 1830002, Apr. 2018. [Online]. Available: www.worldscientific.com

[4] P. Samant, L. Trevisi, X. Ji, and L. Xiang, "X-ray induced acoustic computed tomography," *Photoacoustics*, vol. 19, Sep. 2020, Art. no. 100177.

[5] Y. Zheng et al., "X-ray-induced acoustic computed tomography for guiding prone stereotactic partial breast irradiation: A simulation study," *Med. Phys.*, vol. 47, no. 9, pp. 4386–4395, Sep. 2020. [Online]. Available: https://pubmed.ncbi.nlm.nih.gov/32428252/

[6] M. Wang et al., "Toward in vivo dosimetry for prostate radiotherapy with a Transperineal ultrasound array: A simulation study," *IEEE Trans. Radiat. Plasma Med. Sci.*, vol. 5, no. 3, pp. 373–382, May 2021.

[7] S. Hickling et al., "Ionizing radiation-induced acoustics for radiotherapy and diagnostic radiology applications," *Med. Phys.*, vol. 45, no. 7, pp. e707–e721, 2018.

[8] S. Tang, C. Ramseyer, P. Samant, and L. Xiang, "X-ray-induced acoustic computed tomography of concrete infrastructure," *Appl. Phys. Lett.*, vol. 112, no. 6, Feb. 2018, Art. no. 63504. [Online]. Available: https://aip.scitation.org/doi/abs/10.1063/1.5009936

[9] M. Ahmad, L. Xiang, S. Yousefi, and L. Xing, "Theoretical detection threshold of the proton-acoustic range verification technique," *Med. Phys.*, vol. 42, no. 10, pp. 5735–5744, Oct. 2015. [Online]. Available: /pmc/articles/PMC4567582//pmc/articles/PMC4567582/?report=abstracthttps://www.ncbi.nlm.nih.gov/pmc/articles/PMC4567582/

[10] S. Tang, K. Yang, Y. Chen, and L. Xiang, "X-ray-induced acoustic computed tomography for 3D breast imaging: A simulation study," *Med. Phys.*, vol. 45, no. 4, pp. 1662–1672, Oct. 2018. [Online]. Available: https://pubmed.ncbi.nlm.nih.gov/29479717/

[11] Y. Li, P. Samant, S. Wang, A. Behrooz, D. Li, and L. Xiang, "3D X-ray-induced acoustic computed tomography with a spherical array: A simulation study on bone imaging," *IEEE Trans. Ultrason., Ferroelect., Freq. Control*, vol. 67, no. 8, pp. 1613–1619, Oct. 2020. [Online]. Available: /pmc/articles/PMC7394001/ /pmc/articles/PMC7394001/?report=abstract https://www.ncbi.nlm.nih.gov/pmc/articles/PMC7394001/

[12] Y. Li et al., "The feasibility study of XACT imaging for characterizing osteoporosis," *Med. Phys.*, vol. 46, no. 12, pp. 7694–7702, 2022. [Online]. Available: https://onlinelibrary.wiley.com/doi/full/10.1002/mp.15906 https://onlinelibrary.wiley.com/doi/abs/10.1002/mp.15906 https://aapm.onlinelibrary.wiley.com/doi/10.1002/mp.15906

[13] E. Robertson, P. Samant, S. Wang, T. Tran, X. Ji, and L. Xiang, "X-ray-induced acoustic computed tomography (XACT): Initial experiment on bone sample," *IEEE Trans. Ultrason., Ferroelect., Freq. Control*, vol. 68, no. 4, pp. 1073–1080, Apr. 2021.

[14] L. Xiang, S. Tang, M. Ahmad, and L. Xing, "High resolution X-ray-induced acoustic tomography," *Sci. Rep.*, vol. 6, no. 1, pp. 1–6, Oct. 2016. [Online]. Available: https://www.nature.com/articles/srep26118

[15] L. Xiang, B. Han, C. Carpenter, G. Pratx, Y. Kuang, and L. Xing, "X-ray acoustic computed tomography with pulsed x-ray beam from a medical linear accelerator," *Med. Phys.*, vol. 40, no. 1, 2013, Art. no. 10701. [Online]. Available: https://pubmed.ncbi.nlm.nih.gov/23298069/

[16] W. Zhang, I. Oraiqat, H. Lei, P. L. Carson, I. EI Naqa, and X. Wang, "Dual-modality X-ray-induced radiation acoustic and ultrasound imaging for real-time monitoring of radiotherapy," *BME Front.*, vol. 2020, pp. 1–10, Oct. 2020.

[17] B. Mijnheer, S. Beddar, J. Izewska, and C. Reft, "In vivo dosimetry in external beam radiotherapy," *Med. Phys.*, vol. 40, no. 7, 2013, Art. no. 70903. [Online]. Available: https://pubmed.ncbi.nlm.nih.gov/23822404/

[18] T. Kron, J. Lehmann, and P. B. Greer, "Dosimetry of ionising radiation in modern radiation oncology," *Phys. Med. Biol.*, vol. 61, no. 14, pp. R167–R205, Oct. 2016. [Online]. Available: https://pubmed.ncbi.nlm.nih.gov/27351409/

[19] P. Samant, L. M. Trevisi, Y. Chen, T. Zwart, and L. Xiang, "3-D Protoacoustic imaging through a planar ultrasound array: A simulation Workflow," *IEEE Trans. Radiat. Plasma Med. Sci.*, vol. 7, no. 1, pp. 83–95, Jan. 2023.

[20] F. Alsanea, V. Moskvin, and K. M. Stantz, "Feasibility of RACT for 3D dose measurement and range verification in a water phantom," *Med. Phys.*, vol. 42, no. 2, pp. 937–946, Feb. 2015.

[21] Z. Jiang, L. Sun, W. Yao, Q. J. Wu, L. Xiang, and L. Ren, "3D in vivo dose verification in prostate proton therapy with deep learning-based proton-acoustic imaging," *Phys. Med. Biol.*, vol. 67, no. 21, Nov. 2022, Art. no. 215012. [Online]. Available: https://pubmed.ncbi.nlm.nih.gov/36206745/

[22] H. Paganetti, "Range uncertainties in proton therapy and the role of monte carlo simulations," *Phys. Med. Biol.*, vol. 57, no. 11, pp. R99–R117, Oct. 2012. [Online]. Available: https://pubmed.ncbi.nlm.nih.gov/22571913/

[23] P. K. Pandey, H. O. Aggrawal, S. Wang, K. Kim, A. Liu, and L. Xiang, "Ring artifacts removal in X-ray-induced acoustic computed tomography," *J. Innovat. Opt. Health Sci.*, vol. 15, no. 3, May 2022, Art. no. 2250017. [Online]. Available: www.worldscientific.com

[24] P. K. Pandey, S. Wang, H. O. Aggrawal, K. Bjegovic, S. Boucher, and L. Xiang, "Model-based X-ray-induced acoustic computed tomography," *IEEE Trans. Ultrason., Ferroelectr., Freq. Control*, vol. 68, no. 12, pp. 3560–3569, Dec. 2021.

[25] S. Tang et al., "X-ray-induced acoustic computed tomography with an ultrasound transducer ring-array," *Appl. Phys. Lett.*, vol. 110, no. 10, Oct. 2017, Art. no. 103504. [Online]. Available: https://aip.scitation.org/doi/abs/10.1063/1.4978049

[26] K. C. Jones et al., "Experimental observation of acoustic emissions generated by a pulsed proton beam from a hospital-based clinical cyclotron," *Med. Phys.*, vol. 42, no. 12, pp. 7090–7097, Oct. 2015. [Online]. Available: https://pubmed.ncbi.nlm.nih.gov/26632062/

[27] J. Sun, B. Zhang, Q. Feng, H. He, Y. Ding, and Q. Liu. "Photoacoustic wavefront shaping with high signal to noise ratio for light focusing through scattering media," 2019. [Online]. Available: www.nature.com/scientificreports

Authorized licensed use limited to: Access paid by The UC Irvine Libraries. Downloaded on January 04,2024 at 23:51:20 UTC from IEEE Xplore. Restrictions apply.

[28] S. Wang, V. Ivanov, P. K. Pandey, and L. Xiang, "X-ray-induced acoustic computed tomography (XACT) imaging with single-shot nanosecond x-ray," *Appl. Phys. Lett.*, vol. 119, no. 18, Oct. 2021, Art. no. 183702. [Online]. Available: https://aip.scitation.org/doi/abs/10.1063/5.0071911

[29] P. B. Patil and M. S. Chavan, "A wavelet based method for denoising of biomedical signal," in *Proc. Int. Conf. Pattern Recognit. Inform. Med. Eng.*, 2012, pp. 278–283.

[30] I. Daubechies, "Ten lectures on wavelets," *Ten Lectures Wavelets*. Philadelphia, PA, USA: SIAM, Oct. 1992.

[31] P. S. Addison, "Wavelet transforms and the ECG: A review," *Physiol. Meas.*, vol. 26, no. 5, pp. R155–R199, Oct. 2005. [Online]. Available: https://pubmed.ncbi.nlm.nih.gov/16088052/

[32] B. Choi, J. S. Nelson, J. Spanier, J. A. Viator, and M. Ambrose, "In vivo port-wine stain depth determination with a photoacoustic probe," *Appl. Opt.*, vol. 42, no. 16, pp. 3215–3224, Oct. 2003. [Online]. Available: https://opg.optica.org/viewmedia.cfm?uri=ao-42–16–3215&seq=0&html=true https://opg.optica.org/abstract.cfm?uri=ao-42–16–3215 https://opg.optica.org/ao/abstract.cfm?uri=ao-42–16–3215

[33] S. Mallat, *A Wavelet Tour of Signal Processing*. Amsterdam, The Netherlands: Elsevier, 2009.

[34] M. Unser and A. Aldroubi, "A review of wavelets in biomedical applications," *Proc. IEEE*, vol. 84, no. 4, pp. 626–638, Apr. 1996.

[35] S. H. Holan and J. A. Viator, "Automated wavelet denoising of photoacoustic signals for circulating melanoma cell detection and burn image reconstruction," *Phys. Med. Biol.*, vol. 53, no. 12, pp. N227–N236, Oct. 2008. [Online]. Available: https://pubmed.ncbi.nlm.nih.gov/18495977/

[36] F. Y. Rizi, H. A. Noubari, and S. K. Setarehdan, "Wavelet-based ultrasound image denoising: Performance analysis and comparison," in *Proc. Annu. Int. Conf. IEEE Eng. Med. Biol. Soc.*, vol. 2011, 2011, pp. 3917–3920. [Online]. Available: https://pubmed.ncbi.nlm.nih.gov/22255196/

[37] J. Sohn et al., "Wavelet-based protoacoustic signal denoising for proton range verification," vol. 11319, pp. 14–19, Mar. 2020. [Online]. Available: https://www.spiedigitallibrary.org/conference-proceedings-of-spie/11319/1131904/Wavelet-based-protoacoustic-signal-denoising-for-proton-range-verification/10.1117/12.2550768. full https://www.spiedigitallibrary.org/conference-proceedings-of-spie/11319/1131904/Wavelet-based-protoacoustic-signal-denoising-for-proton-range-verification/10.1117/12.2550768.short

[38] D. L. Donoho and I. M. Johnstone, "Ideal spatial adaptation by wavelet shrinkage," vol. 81, no. 3, pp. 425–455, 1994. [Online]. Available: https://academic.oup.com/biomet/article/81/3/425/256924

[39] "A really friendly guide to wavelets." 1999. [Online]. Available: https://www.polyvalens.com

[40] W. K. Ngui, M. S. Leong, L. M. Hee, and A. M. Abdelrhman, "Wavelet analysis: Mother wavelet selection methods," *Appl. Mech. Mater.*, vol. 393, pp. 953–958, Sep. 2013.

[41] S. G. Mallat, "A theory for Multiresolution signal decomposition: The wavelet a theory for Multiresolution signal decomposition: The wavelet representation." Accessed: Oct. 17, 2022. [Online]. Available: https://repository.upenn.edu/cis_reports

[42] M. Misiti, Y. Misiti, G. Oppenheim, and J.-M. Poggi. "Wavelet toolbox-4 user's guide." 1997. [Online]. Available: www.mathworks.com

[43] F. Adamo, G. Andria, F. Attivissimo, A. M. L. Lanzolla, and M. Spadavecchia, "A comparative study on mother wavelet selection in ultrasound image denoising," *Measurement*, vol. 46, no. 8, pp. 2447–2456, 2013.

[44] D. Kwon, M. Vannucci, J. J. Song, J. Jeong, and R. M. Pfeiffer, "A novel wavelet-based thresholding method for the pre-processing of mass spectrometry data that accounts for heterogeneous noise," *Proteomics*, vol. 8, no. 15, pp. 3019–3029, 2008.

[45] A. M. Atto, D. Pastor, and G. Merciers, "Wavelet shrinkage: Unification of basic thresholding functions and thresholds," *Signal Image Video Process.* , vol. 5, no. 1, pp. 11–28, Oct. 2009. [Online]. Available: https://link.springer.com/article/10.1007/s11760–009–0139-y

[46] R. M. Haralick, S. R. Sternberg, and X. Zhuang, "Image analysis using mathematical morphology," *IEEE Trans. Pattern Anal. Mach. Intell.*, vol. PAMI-9, no. 4, pp. 532–550, Jul. 1987.

[47] M. Xu and L. V. Wang, "Universal back-projection algorithm for photoacoustic computed tomography," *Phy. Rev. E, Statist. Nonlinear Soft Matter Phys.*, vol. 71, no. 1, Oct. 2005, Art. no. 16706. [Online]. Available: https://pubmed.ncbi.nlm.nih.gov/15697763/

[48] B. E. Treeby and B. T. Cox, "k-wave: MATLAB toolbox for the simulation and reconstruction of photoacoustic wave fields," *J. Biomed. Opt.*, vol. 15, no. 2, 2010, Art. no. 21314. [Online]. Available: https://pubmed.ncbi.nlm.nih.gov/20459236/

[49] L. Sun et al., "K-wave simulations and their biomedical application in XACT imaging," vol. 11602, pp. 196–204, Oct. 2021. [Online]. Available: https://www.spiedigitallibrary.org/conference-proceedings-of-spie/11602/116020X/K-wave-simulations-and-their-biomedical-application-in-XACT-imaging/10.1117/12.2579809.full https://www.spiedigitallibrary.org/conference-proceedings-of-spie/11602/116020X/K-wave-simulations-and-their-biomedical-application-in-XACT-imaging/10.1117/12.2579809.short

[50] W. Choi, D. Oh, and C. Kim, "Practical photoacoustic tomography: Realistic limitations and technical solutions," *J. Appl. Phys.*, vol. 127, no. 23, Oct. 2020, Art. no. 230903. [Online]. Available: https://aip.scitation.org/doi/abs/10.1063/5.0008401

[51] R. F. Laine, G. Jacquemet, and A. Krull, "Imaging in focus: An introduction to denoising bioimages in the era of deep learning," *Int. J. Biochem. Cell Biol.*, vol. 140, Nov. 2021, Art. no. 106077.

[52] R. Fisher, *Statistical Methods for Research Workers.*, 13th ed. New York, NY, USA: Hafner, 1958.

[53] D. I. D. Vilimek et al., "Comparative analysis of wavelet transform filtering systems for noise reduction in ultrasound images." 2022. [Online]. Available: https://doi.org/10.1371/journal.pone.0270745

[54] D. L. Donoho and I. M. Johnstone, "Adapting to unknown smoothness via wavelet shrinkage," *J. Amer. Statist. Assoc.*, vol. 90, no. 432, pp. 1200–1224, 1995.

[55] F. Xiao and Y. Zhang, "A comparative study on Thresholding methods in wavelet-based image denoising," *Procedia Eng.*, vol. 15, pp. 3998–4003, Oct. 2011.

[56] N. Verma and A. K. Verma, "Performance analysis of wavelet thresholding methods in denoising of audio signals of some Indian musical instruments," *Int. J. Eng. Sci. Technol.*, vol. 4, no. 5, pp. 2047–2052, 2012.

[57] D. Lee et al., "GPU-accelerated 3D volumetric X-ray-induced acoustic computed tomography," *Biomed. Opt. Exp.*, vol. 11, no. 2, pp. 752–761, 2020. [Online]. Available: https://doi.org/10.1364/BOE.381963

Authorized licensed use limited to: Access paid by The UC Irvine Libraries. Downloaded on January 04,2024 at 23:51:20 UTC from IEEE Xplore. Restrictions apply.